Water-Dynamics Monitoring Using a Flexible Resistive Sensor and Reservoir Computing

Naruhito Seimiya, Koh Uehara, Haruki Nakamura, Guren Matsumura, Takuma Miyashita, Kohei Nakajima, Kuniharu Takei**

N. Semiya, H. Nakamura, T. Miyashita, K. Takei

Graduate School of Information Science and Technology, Hokkaido University, Sapporo, Hokkaido 060-0814, Japan

takei@ist.hokudai.ac.jp

K. Uehara, K. Nakajima

Graduate School of Information Science and Technology, University of Tokyo, Tokyo 113-8656, Japan

k-nakajima@isi.imi.i.u-tokyo.ac.jp

G. Matsumura

Department of Physics and Electronics, Osaka Metropolitan University, Sakai, Osaka 599-8531, Japan

Keywords: Water dynamics, Flexible sensors, Rain sensors, Echo state network, Superhydrophobic

Water droplets exhibit different dynamics upon contact with an object, depending on several factors, including the impact angle and droplet volume. Insights gained from monitoring the dynamics might be valuable in rain-sensing applications for analyzing precipitation and wind

velocity. Notably, a resistive-type flexible rain sensor exists, which monitors the changes in resistance with time when a water droplet contacts an object. However, the dynamics sensing mechanism for water droplets contacting a conductive superhydrophobic surface has not been systematically explored, and importantly, the sensors can only be used at a 20° tilt angle. Therefore, this study aims to reveal the sensing mechanism of resistive sensors by analyzing the vertical energy of water droplets impacting the sensor surface. By varying the conditions surrounding the vertical impact, we observe that the minimum resistance of the sensor to water droplets increases when the impact energy decreases at different dropping heights and sensor tilt angles. Further, a reservoir-computing algorithm is developed to assess the water dynamics at different sensor tilt angles, resulting in the successful estimation of the water-droplet volume and wind velocity.

1. Introduction

Water droplets exhibit unique mechanical properties when contacting a solid object, owing to their liquid phase and surface tension. Over time, the water-droplet deformation dynamics can be studied to obtain a variety of information, including the droplet volume and collision angle. Monitoring the dynamics may provide insights for analyzing environmental conditions from rain droplets, such as wind and rain precipitation. However, because the dynamics of water droplets is complicated[1-3], it is difficult to rapidly analyze the conditions of its contact with solid objects. Recently, machine learning algorithms have gained widespread adoption, and they have been applied to analyze complicated sensor-output changes with relatively high accuracy. One potential machine learning model for monitoring water-droplet dynamics for real-time environmental sensing is the echo state network (ESN), which is one of the seminal networks in reservoir computing. This ESN only tunes the weight of the output layer, facilitating simple and fast estimations [4-7]. To exploit machine learning or some other data-analysis methods, repeatable and stable water-formation monitoring is required. High-speed camera capturing is a viable approach for monitoring droplet deformation, as the camera can capture details of the water dynamics when it encounters an object. However, such camera setups are large and expensive, limiting their widespread application. As a solution, researchers have attempted to develop a simple system comprising a rain sensor (a flexible conductive sensor) and a machine learning algorithm[2]. With this system, the electrical resistance change between a pair of superhydrophobic electrodes was recorded, and the resistance change was analyzed using an ESN. The results depicted that the wind and volume properties of water droplets can be estimated by monitoring the change in electrical resistance within roughly 10 ms of the droplet impact . However, to estimate these values, the tilt angle of the sensor must be set at 20°. Sensors for weather monitoring or other environmental tasks, designed to be attached to a variety of objects regardless of the tilt angle, are considered more convenient and practical. Furthermore, the sensing mechanism for resistance variations when a water droplet collides with an object has not been systematically studied.

To overcome these challenges, this study aims to elucidate the sensing mechanism by varying the vertical energy of water droplets impacting the sensor experimentally. The surface conditions, particularly the contact angle (CA), sliding angle (SA), and CA hysteresis (CAH), of the sensor (LIG/PDMS and PDMS) are also investigated to support the mechanism exploration. An ESN is employed to estimate the water volume and wind velocity at several tilt angles. An optimal algorithm is developed based on the measurement results of complicated water-droplet conductance variations between a pair of electrodes. Furthermore, for comparison, a control experiment is set up where estimations are made without using ESN. The model is also compared with other deep learning models, e.g., transformers. The generalization capability and robustness of the developed sensor system are confirmed by examining the accuracy of volume and wind velocity estimation in real rainwater. The results of this study may facilitate machine learning applications in various laser-induced graphene-based devices[8-12].

Results and Discussion

Superhydrophobic surfaces with insulating PDMS and conductive LIG/PDMS layers were formed by texturizing the surfaces using laser scanning (Figure 1a). The details of the process are described in Method and Figure S1. The LIG patterns were designed by programming a laser cutter tool, and it was transferred onto the PDMS layer. The sensor was equipped with a pair of superhydrophobic conductive LIG/PDMS electrodes with a 0.5 mm gap. When a water droplet hits the pair of electrodes, a closed electrical circuit forms, after which the resistance value can be measured. The resistance varies for a short period (approximately milliseconds), corresponding to the deformation of water droplets on the surfaces of PDMS and LIG/PDMS. This change in resistance over time shows different dynamics depending on the size of the water droplets, wind velocity, and sensor tilt (Figure 1b). Using a high-speed data logger, this electrical response is measured at a sampling rate of 10 kHz. Due to equipment limitation, the circuit is termed open when the resistance is >5 MΩ. The wettability of the sensor surface and the performance of the sensor in water droplets at room temperature of ~20°C were investigated.

First, the wetting behaviors of the water droplet on the PDMS and LIG/PDMS layers were investigated by measuring CA, SA, and CAH. The surface texturization of the PDMS and LIG/PDMS surfaces to form periodic patterns with ~200 μm pitch was achieved by laser scanning (Figures 2a–b). Due to the porosity of LIG, LIG/PDMS exhibited a rougher surface in the periodic pattern than pure PDMS (Figure 2a). The CA (θ), SA (φ), and CAH (θ_A–θ_R) (where θ_A is the angle for advancing CA and θ_R is that for receding CA) were defined as described in Figure 2c-d. All data were measured and extracted using a specialized measurement tool (see Method for more information). The representative CAs for PDMS and LIG/PDMS with and without surface texturization are displayed in Figure 2e. The pristine PDMS surface shows an average CA of 109 ± 2.8°, whereas that of the surface-textured PDMS, which is often defined as a superhydrophobic surface, is 176° ± 3.9°. This large CA improvement is caused by the surface roughness, explained as the Lotus effect described by the

Cassie–Baxter model[13-14]. Similarly, LIG/PDMS shows CA improvements after laser texturization from 138° ± 5.9° to 179° ± 0.1°. Notably, the CA for LIG/PDMS is higher than that for the pristine PDMS because of the difference in the surface roughness caused by the porous LIG layer on PDMS (Figure 2a–b). Next, the relationship between the CA and SA was assessed for the samples subjected to laser texturization (Figure 2f). Although the CAs are almost identical for the LIG/PDMS and PDMS surfaces, the SA values are different at approximately 2.8° ± 0.5° and 9.2° ± 0.6°, respectively, mostly attributed to the difference in the surface roughness. Notably, water does not slide on LIG/PDMS and PDMS without texturization even at φ = 90° (Figure S2). For further investigations of the water adhesion to the surfaces, the CAH when a water droplet starts sliding, as described in Figure 2d, was measured. The CAH for the surface of the textured LIG/PDMS is close to zero (0.7° ± 0.8°), indicating that the water droplets are not pinned on the LIG/PDMS surface; conversely, the CAH is 27.0° ± 7.1° for the texture PDMS surface (Figure 2g). Based on these SA and CAH results, it can be concluded that water droplets adhere strongly to the flat region between the laser-texturized patterns with 200 μm pitch for the texturized PDMS surface (Figure 2b), whereas the small randomly roughened LIG/PDMS surface exhibits poor surface adhesion to water droplets due to weak water-pinning effect.

The mechanism of resistance change when a water droplet collides with a pair of electrodes is discussed. Figure 3a displays the time series deformation of a water droplet (40 μL) once it collides with the sensor at a tilt angle of 20°. The figure depicts that the water droplet spreads rapidly in a radial pattern, recedes, and moves away from the sensor because of the superhydrophobicity and low sliding-angle properties of the sensor surface. Owing to this behavior, the lowest sensor resistance is always obtained at the moment of collision, after which it increases with time (Figure 3b). To understand the detection mechanism of this sensor, we first studied the vertical impact force of the water droplets on the sensor by varying the dropping height from the sensor at tilt angle $\varphi = 0°$. The water-droplet volume (30 μL) was controlled precisely using a micropipette. In this study, the vertical impact energy of E_{impact} is defined as

$$E_{impact} = E_{kine} + E_{surf,} \tag{1}$$

where E_{kine} is the kinetic energy and E_{surf} is the surface energy of the water droplet [15]. The terms on the right side are expressed as follows:

$$E_{kine} = \frac{1}{2}\rho_d V U^2 , \tag{2}$$

$$E_{surf} = \pi d_0^2 \sigma_{ig}, \tag{3}$$

where ρ_d, V, U, d_0, and σ_{ig} are the water density (kg/m^3), droplet volume (m^3), impact velocity in the vertical direction of the sensor (m/s), droplet diameter (m), and surface energy density of liquid (J/m^2), respectively.

The time series plot of the resistance changes depicts a trend: the higher the height (i.e., higher E_{impact}), the lower the resistance values at the moment of impact, although some variations even under the same conditions are observed (Figure 3c–d). In the sensor dynamics, for example, some data from a height of 200 mm have a higher resistance than 150 mm at some point after impact, even though the resistance is lower than 150 mm at the moment of impact (Figure 3c). This is most likely due to the variation of measurements due to misalignment of droplet position on the sensor. This variation should make lower accuracy for the estimation, andthis must be improved in the future. Notably, when the water droplet slides over the sensor region without impact, the resistance value is considerably high, ranging from ~20 to 40 MΩ (i.e., vertical impact energy = 0.003 mJ) (Figure 3d). This reveals that the vertical impact energy plays an important role in this sensing mechanism. For further analyses, the duration for which a water droplet contacts a sensor surface, i.e., the contact time, was investigated. Generally, the contact time depends on the droplet radius r and is fitted by $r^{1.5}$, whereas it is independent of the impact velocity of the droplet [3]. The the contact time extracted from the sensor resistance <5 MΩ was related to $r^{1.35}$ in this experiment (Figure S3a). This minor difference compared with the previous report [3] is obtained probably because the position of the water droplet over the electrodes was not perfectly centered, resulting in slightly fluctuating results. Furthermore, it is confirmed that the impact velocity of the droplet does not affect the on-state time, which is consistent with previous reports [3] (Figure S3b). Next, to systematically confirm the role of the vertical impact force, the tilt-angle dependence was examined at a constant water volume (30 μL) and dropping height (150 mm). Owing to gravity, the vertical impact force changes as a function of the sensor's tilt angle, indicating that the minimum resistance at low tilt angles is small (Figure 3e-f).

The impacting water droplet receives a repulsive force from the air layer trapped in the rough concave surface, and when the water droplet achieves the highest sinking depth into the rough surface, the velocity in the vertical direction to the sensor becomes zero. Therefore, the vertical impact energy of the water droplet to the sensor changes the amount of water sinking into the rough surface of the sensor. Based on this water behavior over the rough surface, the sensing mechanism can be described, as shown in Figure 3g. The sensor resistance is expressed as the sum of the water resistance (R_w) and the contact resistance (R_c). R_c is expressed as

$$R_C \propto \frac{1}{A_C}, \tag{4}$$

where A_C is the contact area between the LIG/PDMS surface and a water droplet. R_w is negligibly sufficiently low compared to R_c. When water slides down over the sensor, corresponding to low vertical impact energy, the contact area A_{C1} is small, attributed to the superhydrophobic surface. This results in a high contact resistance, R_{C1}. In contrast, the contact area A_{C2} at the moment of impact on the sensor is larger because of the high vertical impact energy. Correspondingly, the contact resistance, R_{C2}, is lower than R_{C1}. This suggests that the vertical impact force is stronger than the force induced by superhydrophobicity to push water up over the rough LIG/PDMS structure. Furthermore, to evaluate the effect of temperature on time series plots, the resistance of water droplets at temperature from 20°C to 45°C using a droplet volume of 30 μL, a wind velocity of 0 m/s, and a tilt of 20° were measured (Figure S4). As the temperature increased, the rise in resistance was slower. This is thought to be due to a change in the state of the interface between the water droplet and the sensor, such as a decrease in repulsive force, caused by a decrease in the surface tension, viscosity, and density of water due to an increase in temperature. Since there is temperature dependence for the resistance change, the sensor system should be developed that is compatible with the different temperature droplet in future.

Considering the sensing mechanism, resistance change should be observed at different sensor tilt angles and droplet volumes, owing to the different vertical impact forces on the sensor and the water behaviors on the sensor. Figure 4a–b displays the continuous high-speed camera photos captured at wind velocities of 0 and 5 m/s. As wind flow changes the incidence angle of the water droplet, the vertical impact force changes, which in turn influences the resistance change. As expected, depending on the volume of water droplet, wind velocity, and tilting angle, different time series plots of the resistance are observed, as shown in Figure 4c. Due to the clear differences in the time series plots of the resistances depending on the conditions, the droplet volume and wind velocity can most likely be extracted by analyzing the singularity of resistance changes.

ESN was applied to estimate the water-droplet volume and wind velocity at multiple sensor tilt angles. Using this ESN, a multitask system algorithm for volume and wind velocity estimations was developed (Figure 5a). In this system, the ESN algorithm was optimized for volume target $\hat{y}^{vol}$ and wind velocity target $\hat{y}^{wind}$, and it estimated the volume and wind velocity outputs, $y(= y^{vol} + y^{wind}) \in \mathbb{R}^{N_y}(N_y = 2)$, simultaneously. The detailed modeling and analyses of ESN are described in Method. Accordingly, 336 datasets (7 data samples per sensor tilt, volume, and wind velocity, as shown in Figure 4c) were employed to estimate the volume and wind velocity of the water droplets at multiple sensor tilt angles ranging from 0° to 60°. Due to the difficulty of analyzing all tilt data simultaneously, which is discussed later, the datasets were separated into 84 data samples for each sensor tilt angle. Among the 7 data samples for each condition, the samples were divided into 5 training and 2 test sets, totaling 60 training and 24 test sets. To avoid fitting to specific training and test sets, threefold cross-validation was implemented. Additionally, to prevent overfitting and improve accuracy, data augmentation was conducted by introducing Gaussian noise with a mean of zero and a standard deviation of 0.1 to the training data, resulting in an increase in the observations to 1560. After data augmentation, natural logarithm transformation was performed on the training and test data (Figure S5). For the system evaluation, the normalized mean squared error (NMSE) was evaluated using the below equation to compare the performance between different hyperparameters.

$$\mathrm{NMSE} = \frac{\sum_{m=1}^{M}(y_m - \hat{y}_m)^2}{\sum_{m=1}^{M}(\hat{y}_m - \bar{y}_m)^2} \ , \tag{5}$$

where y_m, $\hat{y}_m$, and $\bar{y}_m$ are the estimated value, target value, and average target value, respectively. The NMSEs were obtained from the cross-validation of the three different pairs of training and test datasets (NMSE_1, NMSE_2, and NMSE_3), and the $\mathrm{NMSE}_{\mathrm{CV}}$ was calculated from these averages as follows:

$$\mathrm{NMSE}_{\mathrm{CV}} = \frac{\mathrm{NMSE}_1 + \mathrm{NMSE}_2 + \mathrm{NMSE}_3}{3}, \tag{6}$$

The hyperparameters (reservoir node N_x, time-multiplexing L, spectral radius SR, and input magnitude IM) of the ESN were optimized by grid search for each sensor tilt angle (Figure S6). The time-multiplexing parameter, L, denotes the time taken to collect the reservoir node (details are provided in Method). The optimum hyperparameters were determined as those that afforded the smallest $\mathrm{NMSE}_{\mathrm{Average}}$, which is the average of the $\mathrm{NMSE}_{\mathrm{CV}}$ of the volume and wind velocity calculated in Equations (5) and (6). Figure S6a shows the $\mathrm{NMSE}_{\mathrm{Average}}$ for different N_x and L values. Here, to avoid prolonged search time due to an increase in the number of parameters, the N_x and L parameters were searched at SR = 1.5 and IM = 0.8. The optimal reservoir node extracted from the grid search was $N_x = 5$ for a tilt angle of 40° and $N_x = 10$ for other tilts, and the optimal time-multiplexing parameter was $L = 45$ for a tilt angle of 20°, $L = 90$ for 40°, and $L = 60$ for the other tilt angles. Next, using the optimal time-multiplexing and the reservoir node values, grid searches for the *SR* and the *IM* were performed, and the values that minimize the $NMSE_{Average}$ were selected as the optimal parameters (Figure S6b-c). At $SR > 1$, where the echo state property (ESP) [16] is not satisfied in general, a relatively low $NMSE_{Average}$ is obtained. To increase accuracy even at $SR > 1$, the initial value in this study was fixed to 0 to make the ESN response reproducible against the identical input series, allowing the rich expressivity of chaos to be exploited for learning. However, increasing *SR* further results in overfitting, increasing $NMSE_{Average}$ drastically. In fact, comparing the reservoir dynamics at a 60° tilt and $IM = 0.5$ for different *SR* values, the dynamics at the transient state of the input showed a more complex trajectory as *SR* increased (Figure S7). Subsequently, at the steady state of the input, a steady trajectory was observed at $SR \leqq 1.4$, whereas a chaotic trajectory was observed at $SR = 2.0$. The *IM* has the property of suppressing the chaos of the reservoir dynamics enhanced by the spectral radius. Comparing the reservoir dynamics between $IM = 0.1$ and 0.5, the reservoir dynamics at $IM = 0.1$ showed a chaotic trajectory even at the steady state of the input. After grid search, the optimal hyperparameters of *IM* and *SR* were determined to be 0.5 and 1.4, respectively. Figure 5b shows the estimated volume and wind velocity for each sensor tilt angle using the optimized hyperparameters (Table S1). Although there are some variation errors for volume estimations, the results were similar regardless of the sensor tilt angles. However, for wind-velocity estimations, slightly large variations in the results were observed. This large variation is most likely caused by the small misalignment of the water droplet on the sensor during the collection of data under wind flow. Furthermore, the wind velocity should fluctuate because the experiment was conducted in a room without a specific wind-flow setup. By collecting more datasets and improving the environment in which the experiment is conducted, the estimation results for both volume and wind velocity can be improved; this will be addressed in future studies. For more quantitative comparisons to estimate the accuracy and effectiveness of ESN, the NMSEs with and without ESN were compared (Figure S8). The detailed analyses without the ESN are explained in Supporting Information Note 1. The $NMSE_{CV}$ values with ESN for all sensor tilts are >1.2 times lower in the volume estimations and >1.7 lower in the wind velocity estimations than those without ESN (Figures 5d and S8). This explains the importance of using ESN for complicated multi-task data analyses. For further comparison, a transformer[17], which is a deep learning architecture suitable for time series analysis, was employed to assess the enhancement of the estimation accuracy (see Supporting Information Note 2 for further details). The model used in this study was composed of four layers: an input, a positional encoder, a transformer encoder, and feed-forward layers (Figure S9). Grid search was implemented to find the optimal hyperparameters (Table S2). Interestingly, the more advanced transformer architecture achieves lower accuracy than the ESN (Figures 5d and S10). This is because the transformer often requires a large amount of training data to improve the accuracy[18]. Similar to transformer, other machine learnings are expected to show lower accuracy than the ESN due to the small number of data[19-20].. Although the accuracy of the transformer can be improved by collecting more datasets, this study proves that ESN for water dynamics analyses achieves relatively good accuracy with a small number of datasets. This result suggests that ESN is suitable for the fast and simple predictions required in local rain sensing.

This system's ability to accurately estimate the water-droplet volume and wind velocity regardless of the sensor tilt angle will promote its application in infrastructures. The possibility of simultaneously estimating volume and wind velocity accurately without considering the sensor tilt was examined for all sensor outputs at different tilt angles. For these analyses, threefold cross-validation was implemented, and in each data group, 6240 datasets (including data augmentation) and 96 datasets were employed for training and testing, respectively. The

NMSE values using the full dataset are ~1.5 times and ~2 times higher for the volume and wind velocity estimations, respectively, compared with those obtained at individual sensor tilt angles (Figures 5d and S11). From these results, we conclude that the sensor estimates the volume of water droplets and wind velocity using the present algorithm with specific hyperparameters for each tilt. This sensor can only estimate the volume of water droplets and wind velocity, but cannot estimate the amount of precipitation. For precipitation estimation, this sensor needs to be integrated to make array structure in the future, and this monitored volume distribution allows to calculate the amount of precipitation per unit time. In real-world conditions, this sensor may be subject to interference due to the superposition effect of water droplets. To reduce this, the contact time between the sensor and the water droplets should be reduced. This contact time can be shortened by texturing the surface with different roughness to break the symmetry of the spreading and shrinking of the droplets[21]. However, because of the symmetry breaking, the change in sensor dynamics due to the shift in drop position is expected to be significant. Therefore, the best approach to the problem of interference due to superposition effects is to make sensor array and eliminate data with interference due to the superposition effect.

Finally, the ability of this sensor system to estimate volume and wind velocity from the impact dynamics of real rainwater droplets containing various dirt and liquids were investigated. The time series of the resistance for a volume of 30 μL, a wind velocity of 0 m/s, and a tilt of 20° in rainwater and tap water were compared (Figure S12a). The data variability was slightly large for rainwater than that of tap water, but both time series of resistance values showed nearly identical trends. Furthermore, Figures S12b-c show the volume and wind velocity estimation results for tap water and rainwater, indicating that volume and wind velocity are estimated with relatively high accuracy for rainwater. Based on these results, we conclude that the sensor system has generalization capability and robustness for rain monitoring.

Conclusions

In this study, the dynamics sensing mechanism of water droplets impacting a conductive superhydrophobic film was investigated, and the droplet volume and wind velocity at different sensor tilt angles were estimated. First, CA, SA, and CAH were measured to assess the surfaces of PDMS and LIG/PDMS before and after texturizations, which are important for realizing reliable water-droplet sensing and understanding the sensing mechanism. The results showed that surface texturing confers superhydrophobic properties on the sensor, resulting in reduced water adhesion. Next, the vertical impact energy dependence was characterized to understand the sensing mechanism. The results revealed that the contact area between the water droplets and the texturized rough LIG/PDMS surface is an essential parameter for effective sensing. This contact area is mostly affected by the balance of forces, i.e., the superhydrophobicity pushing up the water droplet from the sensor surface and the impact energy pushing it down to the sensor surface. The ESN algorithm was optimized for the water volume and wind velocity estimations at different sensor tilt angles, resulting in relatively good estimation accuracies. In addition, the water volume and wind velocity could be estimated with relatively high accuracy in actual rainwater. These results provide insights for understanding the real-time dynamics of water droplets on impact with objects, as well as for local weather monitoring. However, further developments and optimizations for the sensor structure and ESN algorithm are required in the future.

Experimental Section/Methods

Sensor fabrication: A polyimide (PI) film was first exposed to a CO_2 laser and cut using a commercial laser cutting tool (VLS 2.30, Universal Laser System) to convert it into LIG (Figures S1 (1)(2)) [12,22-23]. The laser power was 10 W, and the scanning speed was 254 mm/s at 500 pulses per inch (PPI). A PDMS solution was poured over the LIG/PI film, followed by curing at 90ºC for 90 min (Figure S1 (3)). Next, PDMS was delaminated from the PI film, resulting in the transfer of LIG onto the PDMS film (Figure S1(4)). Thereafter, the surfaces of LIG/PDMS and PDMS were texturized using the same CO_2 laser scanning to create microscopic rough surfaces (Figure S1(5)). Here, the laser power for the texturization was 3.75 W, and the laser speed was 508 mm/s at 500 PPI. These parameters of the laser cutting tool to form the laser-textured LIG/PDMS were selected to realize optimal conductive and superhydrophobic device for water droplet sensors[2].

Characterization of superhydrophobicity: The CA, SA, and CHA measurements and characterizations were performed using a commercially available tool (SmartDrop Plus, Femtobiomed). The SA and CHA were measured by moving the sensor tilt angle at a speed of 0.1°/s.

Echo state network modeling and analyses: The initial value of $x_{\mathrm{k}}(\mathrm{t}) \in \mathbb{R}^{N_x}$ was set at $x_k(0) = 0$, and it is expressed by

$$x_k(t) = \tanh(W x_k(t-1) + W_{in}[1; u_k(t)]), \tag{7}$$

where k $(0 \leq \mathrm{k} < 1560)$ is the number of input data presentations, t $(0 \leq \mathrm{t} \leq 180)$ is time, tanh is a hyperbolic tangent, and $u_k(\mathrm{t}) \in \mathbb{R}^{N_u} (N_u = 1)$ is the external input. The bias term was added to the input $u_k(\mathrm{t})$. $W_{in} \in \mathbb{R}^{N_x \times (1 + N_u)}$ and $W \in \mathbb{R}^{N_x \times N_x}$ are the input and inner weight matrices, respectively. Here, W_{in} is uniformly distributed with $[-\sigma, \sigma]$. The input scaling of σ and the spectral radius of W are hyperparameters. Observational noise according to a normal distribution with a standard deviation of 0.001 was added to the $x_{\mathrm{k}}(\mathrm{t})$ used for learning to avoid multicollinearity in the learning of the readout weights, which will be discussed later. $x_{\mathrm{k}}(\mathrm{t})$ and $u_k(\mathrm{t})$ were recorded at intervals of 180 steps, and they were reconstructed in the spatial direction as nodes $\mathrm{s}_{\mathrm{k}}^{\mathrm{x}} \in \mathbb{R}^{N_x \cdot L}$ and $\mathrm{s}_{\mathrm{k}}^{\mathrm{u}} \in \mathbb{R}^{N_u \cdot L}$, respectively. Here, L is time-multiplexing.

$$\mathrm{s_k^x} = [x_k(1); x_k\,(2); \cdots; x_k\,(L)], \tag{8}$$

$$\mathrm{s_k^u} = [u_k(1); u_k\,(2); \cdots; u_k\,(L)], \tag{9}$$

where $\mathrm{s_k^x}$, $\mathrm{s_k^u}$, and the bias term are concatenated and connected to the output layer as nodes: $X_k \in \mathbb{R}^{N_X}(N_X = (1 + (N_x + 1) \cdot L))$.

$$X_k = [1; \mathrm{s_k^x}; \mathrm{s_k^u}], \tag{10}$$

$$y_k = W_{out}X_k, \tag{11}$$

where $y_k \in \mathbb{R}^{N_y}(N_y = 2)$ and $W_{out} \in \mathbb{R}^{N_y \times N_X}$ are the output and the readout weight, respectively. Ridge regression was applied as a linear learner to prevent overfitting caused by increasing the number of nodes. The training of W_{out} by ridge regression is expressed as follows:

$$W_{out} = (X^T X + \beta I)^{-1} X^T y, \tag{12}$$

where β is the ridge term. The optimal weight W_{out} is $W_{out} = (X^T X)^{-1} X^T y$, obtained by the least squares when β tends to 0, and the optimal weight W_{out} approaches 0 as β approaches infinity. The optimal β was determined by solving the degrees of freedom (*df*), expressed as

$$df = \sum_{i=1}^{N_X} \frac{\lambda_i}{\lambda_i + \beta}, \tag{13}$$

where λ_i is an eigenvalue of $X^T X$. *df* has a one-to-one correspondence with β and varies from 1 to N_X. β and W_{out} were calculated for each value of *df* based on Equations (12) and (13). The residual sum of squares, $\mathrm{RSS} = \sum_{k=0}^{1559}(\hat{y}_k - y_k)^2$, was calculated to obtain Akaike's information criterion (AIC).

$$AIC = M \log(RSS) + 2\,df, \tag{13}$$

where $M = 1560$ is the size of the training data used. By calculating the AIC for each *df*, the optimal β and W_{out} that minimize the AIC were determined.

Statistical analysis: All data were analyzed by collecting certain number of repeated data. The number of datasets and preprocessing for ESN are described in the main text or Figures. Error bars using standard deviation were used for some results.

Supporting Information

Supporting Information is available from the Wiley Online Library or from the author.

Acknowledgements

This work was partially supported by JST AIP Accelerated Program (No. JPMJCR21U1), JST ALCA-Next (No. JPMJAN23F1), JSPS KAKENHI (Grant No. JP22H00594, JP24H00887).

Received: ((will be filled in by the editorial staff))

Revised: ((will be filled in by the editorial staff))

Published online: ((will be filled in by the editorial staff))

References

[1] R. Rioboo, M. Voue, A. Vaillant, J. D. Coninck, *Langmuir : the ACS journal of surfaces and colloids* **2008**, 24, 14074.

[2] S. Wakabayashi, T. Arie, S. Akita, K. Nakajima, K. Takei, *Adv. Mater.* **2022**, 34, 2201663.

[3] D. Richard, C. Clanet, D. Quéré, *Nature* **2002**, 417, 811.

[4] M. Lukosevicius, *Neural Networks: Tricks of the Trade* **2012**, 7700, 659.

[5] M. Lukoševičius, H. Jaeger, *Comput. Sci. Rev.* **2009**, 3, 127.

[6] K. Nakajima, *Jpn. J. Appl. Phys.* **2020**, 59, 060501.

[7] K. Nakajima, I. Fischer, *Springer Nature* **2021**.

[8] Z. Li, Z. Wang, Q. Li, Y. Wang, B. Xiao, Y. Gao, M. Zhu, F. Xuan, *IEEE Sensors J.*, 2024. 10.1109/JSEN.2024.3394572.

[9] Q. Li, R. Bai, Y. Gao, R. Wu, K. Ju, J. Tan, F. Xuan, *ACS Appl. Mater. & Interfaces*, **2021**, 13, 10171-10180.

[10] Y. Lu, G. Yang, S. Wang, Y. Zhang, Y. Jian, L. He, T. Yu, H. Luo, D. Kong, Y. Xianyu, B. Liang, T. Liu, X. Ouyang, J. Yu, X. Hu, H. Yang, Z. Gu, W. Huang, K. Xu, *Nat. Electron.,* **2024**,7, 51–65.

[11] Y. Gao, F. Dong, K. Ju, Q. Li, X. Ling, L. Ma, *IEEE Sensors J.*, **2024**, 24, 750-756.

[12] K. Xu, Z. Cai, H. Luo, Y. Lu, C. Ding, G. Yang, L. Wang, C. Kuang, J. Liu, H. Yang, *ACS Nano* **2024**, 18, 26435-26476 .

[13] K.-Y. Law, *Acc. Mater. Res.* **2022**, 3, 1.

[14] X. He, K. Zhang, X. Xiong, Y. Li, X. Wan, Z. Chen, Y. Wang, X. Xu, M. Liu, Y. Jiang, S. Wang, *Small* **2022**, 18, 2203264.

[15] Y. Yonemoto, T. Kunugi, *Sci. Rep.* **2017**, 7, 2362.

[16] H. Jaeger, *Technical Report GMD Report* **2001**, 148, 1.

[17] A. Vaswani, N. Shazeer, N. Parmar, J. Uszkoreit, L. Jones, A. N. Gomez, L. Kaiser,

I. Polosukhin, *31st Conf. Neural Information Processing Systems (NIPS 2017)* **2017**.

[18] R. Fukushima, J. Tani, *arXiv* **2023**, 2311.10763.

[19] Q. Wen, L. Sun, F. Yang, X. Song, J. Gao, X. Wang, and H. Xu, *arXiv* **2020**, 2002.12478.

[20] L. Taylor, G. Nitschke, *2018 IEEE SSCI*, **2018**, 1542–1547.

[21] J. C. Bird, R. Dhiman, H. M. Kwon, K. K. Varanasi, *Nature*, **2013**, 503,385-388.

[22] J. Lin, Z. Peng, Y. Liu, F. Ruiz-Zepeda, R. Ye, E. L. Samuel, M. J. Yacaman, B. I. Yakobson, J. M. Tour, *Nat. Commun.* **2014**, 5, 5714.

[23] R. Ye, D. K. James, J. M. Tour, *Acc. Chem. Res.* **2018**, 51, 1609.

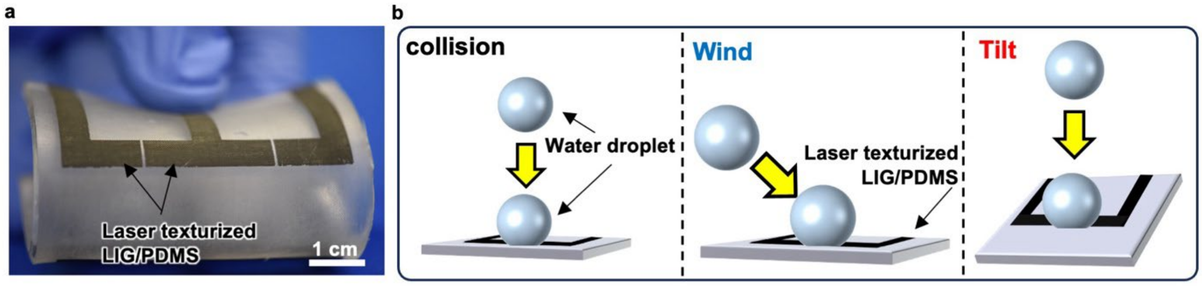

Figure 1. (a) Photo of the superhydrophobic water-droplet sensor sheet. (b) Concept of this study to estimate the volume of water droplet, wind, and tilt.

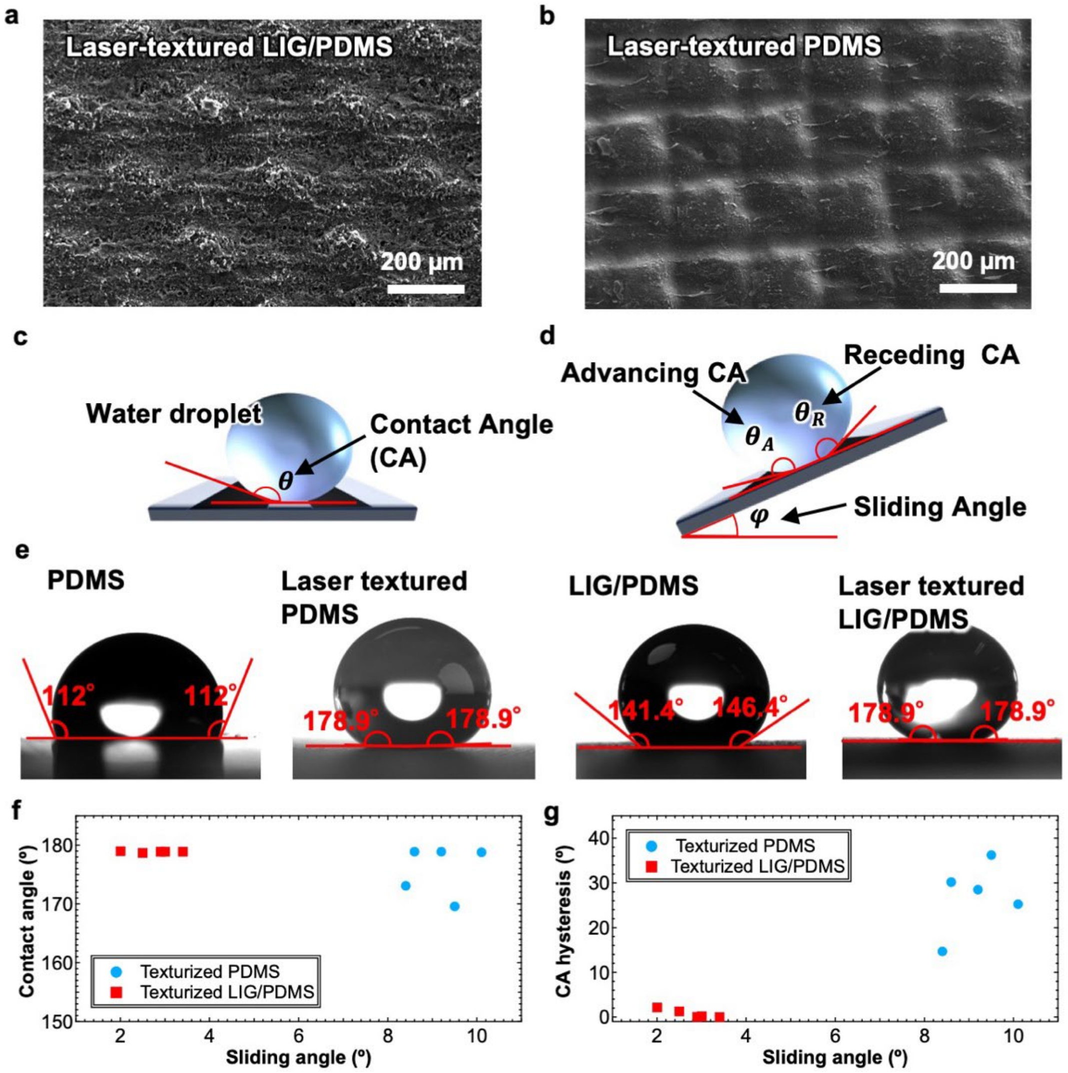

Figure 2. SEM images of the (a) laser-textured LIG/PDMS and (b) laser-textured PDMS. Descriptions of the processes for measuring the (c) contact angle (CA) and (d) sliding angle (SA) and its hysteresis (CAH). (e) Photos of the CA observations on different surfaces: PDMS, laser-textured PDMS, LIG/PDMS, and laser-textured LIG/PDMS from left to right. (f) CAs and (g) contact angle hysteresis (CAH) on textured PDMS and LIG/PDMS at the sliding angles.

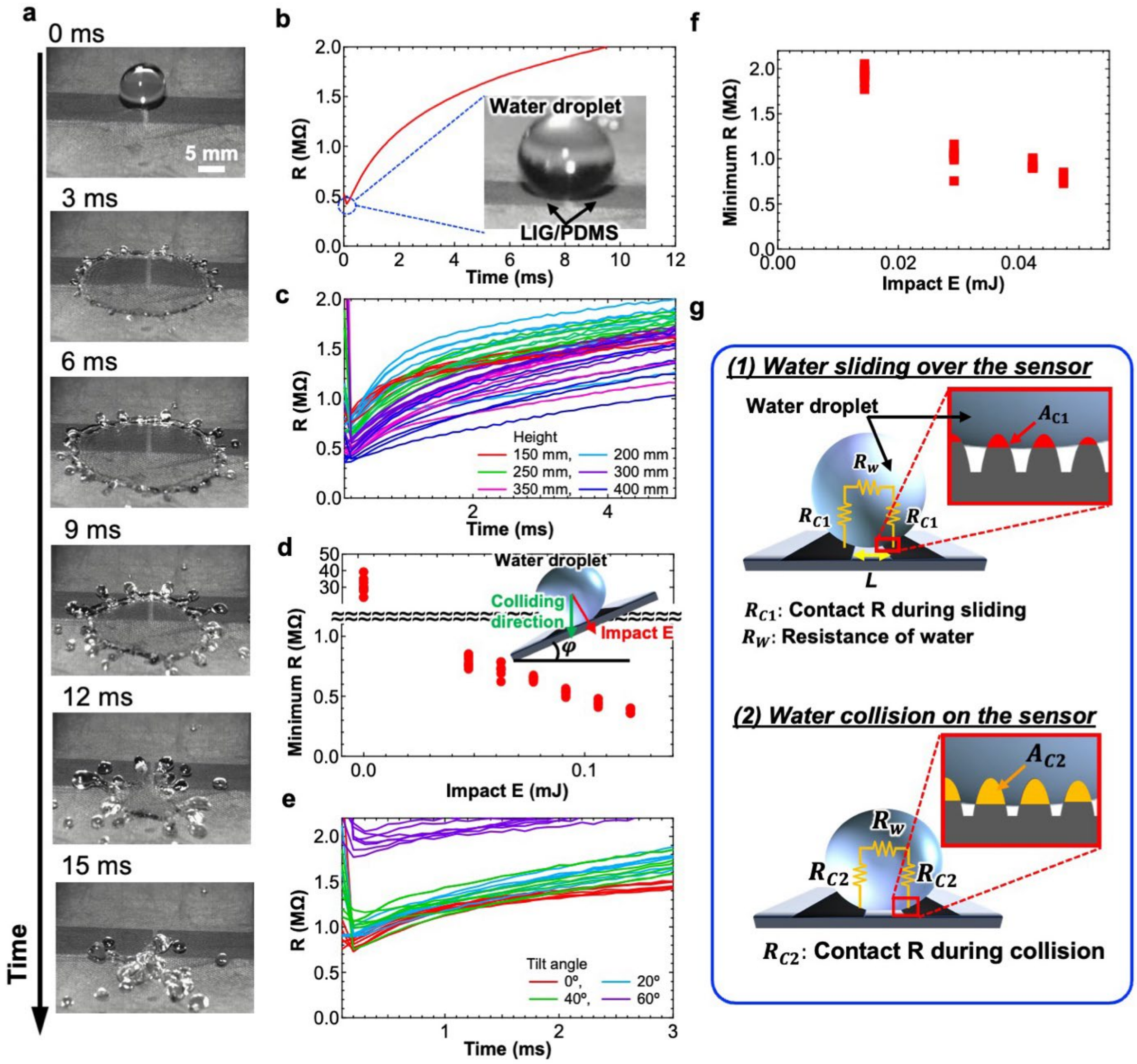

Figure 3. (a) Time series photos after the collision of a water droplet on the sensor. (b) Time series of the resistance changes after the collision of a water droplet on the sensor. Inset: a photo at the moment of water-droplet collision with the sensor. (c) Time series of the resistance at different dropping heights to the sensor surface. (d) Minimum resistance at different impact energies calculated from (c). (e) Time series of the resistance at different sensor tilt angles. (f) Minimum resistance as a function of the impact energy extracted from (e). (g) Detailed sensing mechanism of the sensor considering water sliding and water collision.

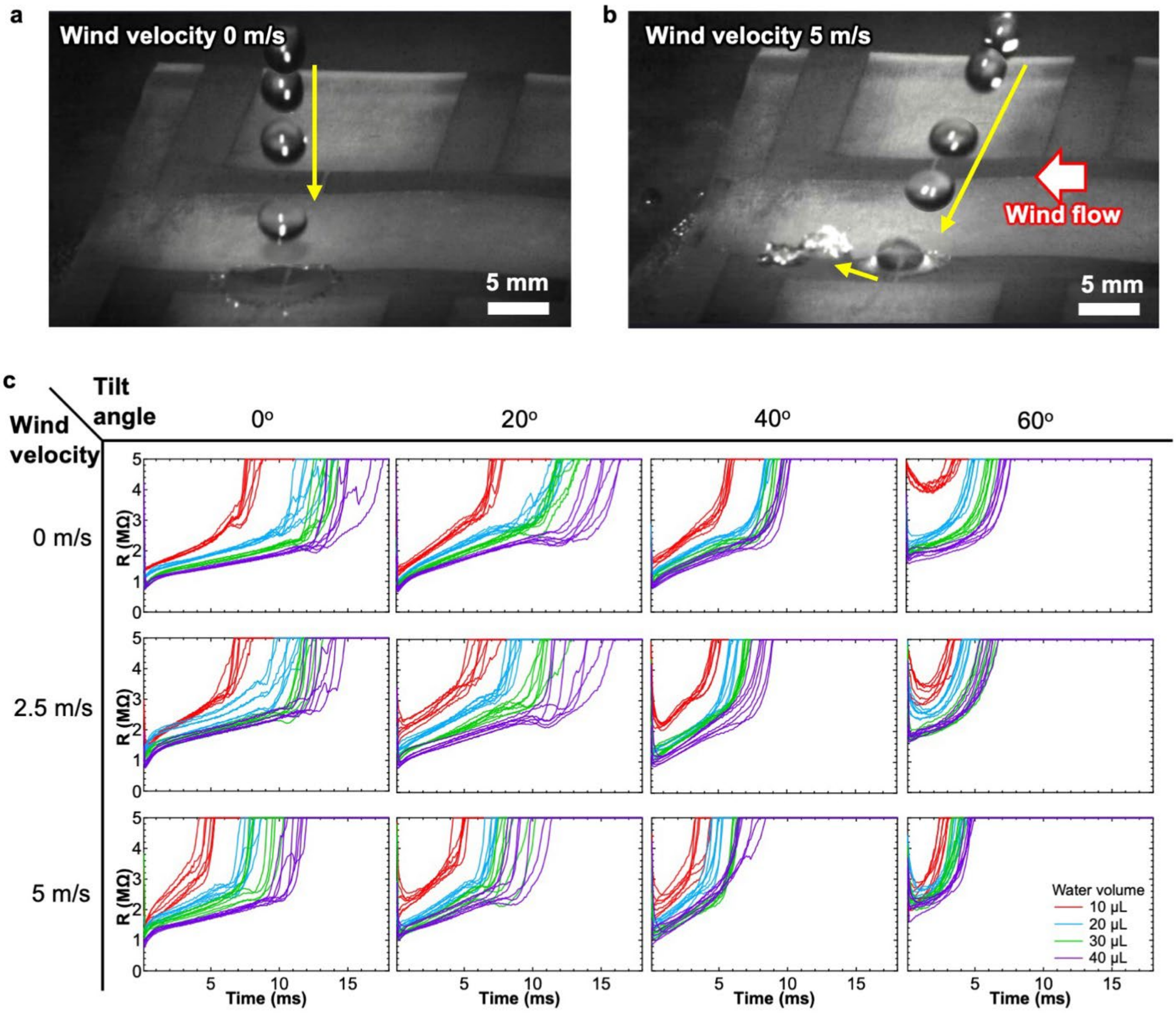

Figure 4. Time series photos of the wind velocity (a) 0 and (b) 5 m/s. (c) Water-droplet dynamics at different wind velocities, volumes, and tilt angles.

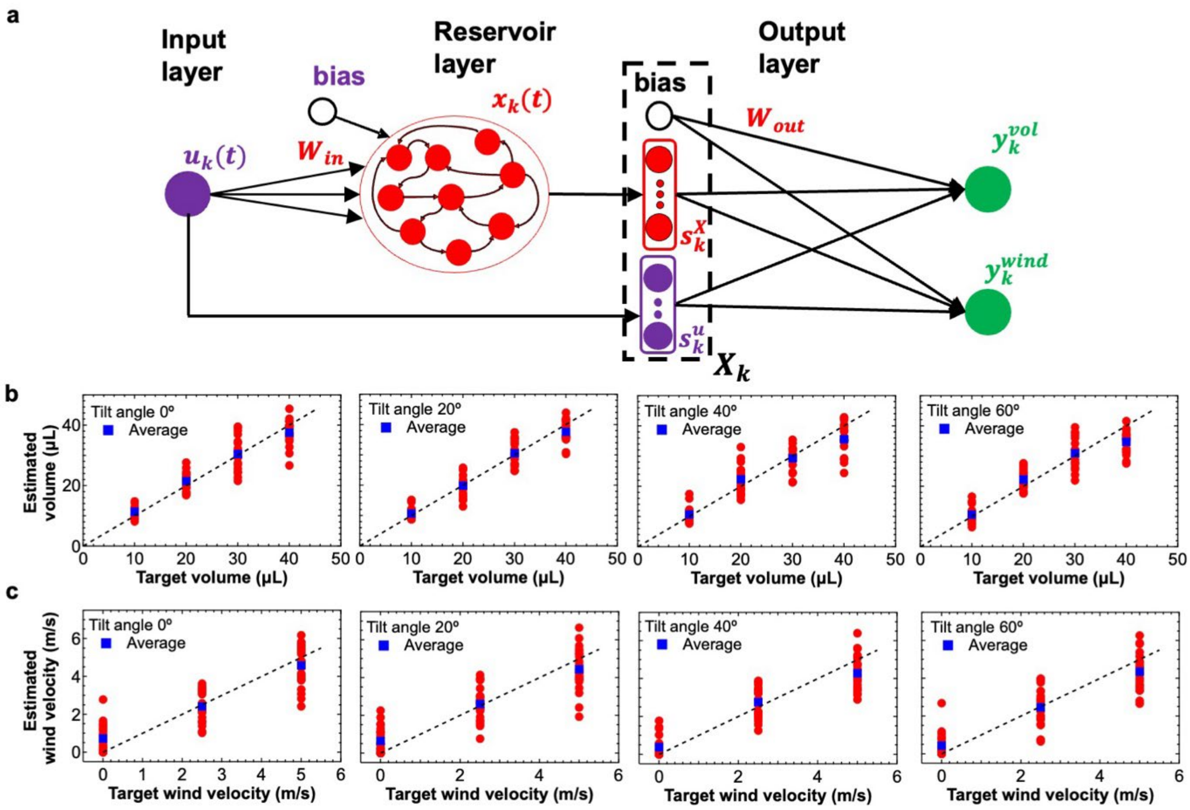

d

	Volume			Wind velocity		
	With ESN	Without ESN	Transformer	With ESN	Without ESN	Transformer
Tilt 0°	0.14481	0.24437	1.0086	0.22317	0.51521	1.0004
Tilt 20°	0.10137	0.17749	1.0189	0.24420	0.60337	1.0000
Tilt 40°	0.19009	0.24048	1.1042	0.18456	0.41058	1.0004
Tilt 60°	0.18095	0.22514	1.0420	0.22099	0.38610	1.0001
All tilt angles	0.30321			0.51057		

Figure 5. (a) Echo state network (ESN) architecture employed in the experiment. (b) Estimated volume against target volume at different sensor tilt angles. (c) Estimated wind velocity against target values at different sensor tilt angles. (d) Compiled results of NMSE at each and all sensor tilt angles with and without ESN. Additionally, the NMSEs obtained using the transformer are added for comparison.

This study reveals the sensing mechanism of water dynamics using a pair of superhydrophobic electrodes analyzed by the vertical impact energy systematically and estimate water droplet volume and wind velocity at different sensor tilt angle using an echo state network by monitoring water droplets dynamics upon contact with an object.

Naruhito Seimiya, Koh Uehara, Haruki Nakamura, Guren Matsumura, Takuma Miyashita, Kohei Nakajima*, Kuniharu Takei*

Water-Dynamics Monitoring Using a Flexible Resistive Sensor and Reservoir Computing

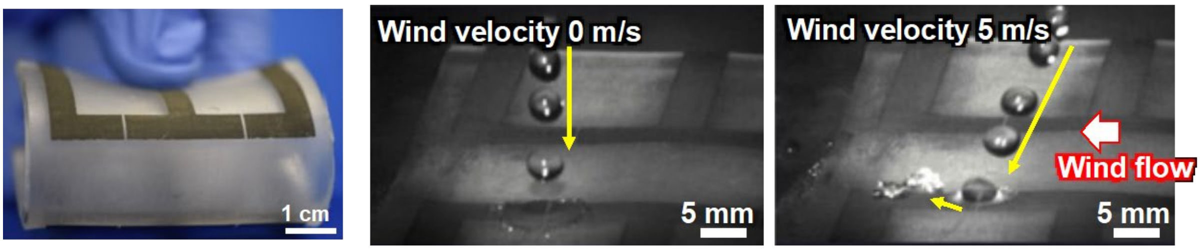

Supporting Information

Water-Dynamics Monitoring Using a Flexible Resistive Sensor and Reservoir Computing

Naruhito Seimiya, Koh Uehara, Haruki Nakamura, Guren Matsumura, Takuma Miyashita, Kohei Nakajima, Kuniharu Takei**

Note 1: Data analyses without using ESN

To demonstrate the validity of the reservoir computing (RC) in this study, the estimated results with RC were compared with those of ridge regression without RC. The ridge regression without RC for the water-droplet volume and wind velocity estimations is expressed as

$$U = [u_k(1); u_k(2); \cdots; u_k(L)]. \tag{8}$$

In Equation (8), we connected u from 1 to L timestep and defined it as node $\mathrm{U} \in \mathbb{R}^{N_u \cdot L}$.

$$y = W_{out}[1; \mathrm{U}]. \tag{9}$$

In Equation (9), the bias is connected to node U. Figure S8 shows the estimated volume and wind velocity at each sensor tilt angle without RC.

Note 2: Data analysis using the transformer

To further demonstrate the validity of RC in this study, the estimated results using RC were compared with those obtained using the transformer architecture. A transformer is a deep learning architecture for sequence-to-sequence training tasks using only an attention mechanism[1]. The attention mechanism calculates the strength of the relationship between the contexts of the input data and allows the transformer to extract features from the entire time series data. On the other hand, other machine learning algorithms, especially convolutional neural network (CNN), does not have a mechanism to compute the positional relationships of the entire data, making them suitable for computing local data dependencies, but difficult to compute the relationships of the entire data. In fact, transformers have been reported to be more accurate than CNN in time-series prediction or classification[2-4].Thus, since the transformer is generally better suited for time series analysis than other machine learning methods, we demonstrated the effectiveness of the ESN algorithm in this study by comparing the transformer results. Figure S9 shows the transformer model employed in this study. Here, only the encoder model was adopted. This model is composed of four layers: an input layer, a positional encoding layer, a transformer encoder layer, and a feed-forward layer. In the input layer, the training of a 180-step sequence of input data with the transformer was divided into 5 sections with 36 steps. Next, the positional encoder assigned positional information to maintain the order relationship of the five intervals. The positional encoding is represented by the following equation[1]:

$$PE_{(pos,2i)} = \sin\left(\frac{pos}{1000^{\frac{2i}{d_{model}}}}\right), \tag{10}$$

$$PE_{(pos,2i+1)} = \cos\left(\frac{pos}{1000^{\frac{2i}{d_{model}}}}\right), \tag{11}$$

where pos, i, and d_{model} are the position, dimension, and length of split data, respectively. The d_{model} was 36 steps in this study. The transformer encoder layers can be stacked to capture the higher and more complex representations, and the number of layers (n_{layers}) is denoted as a hyperparameter. The encoder layer was composed of a multi-head attention layer and a feedforward layer. Here, the multi-head attention plays the role of understanding the expression of the sequence using an Attention structure with multiple heads. The number of heads (n_{head}) is also a hyperparameter. In this study, n_{layers} and n_{head} were optimized by grid search. The optimal hyperparameters for volume and wind velocity estimations at each tilt angle are shown in Table S2. For consistent comparison, the number of dimensions of the feedforward layer in the encoder and output for each tilt are the same as the number of nodes used in the RC. The weights for each layer were trained by minimizing the MSE between the predictions and the target values of volume and wind velocity. A stochastic gradient descent optimizer with a *learning rate* of 0.02, *momentum* of 0.5, and $weight_{decay}$ of 0.005 was adopted, and the model was trained for 40 epochs.

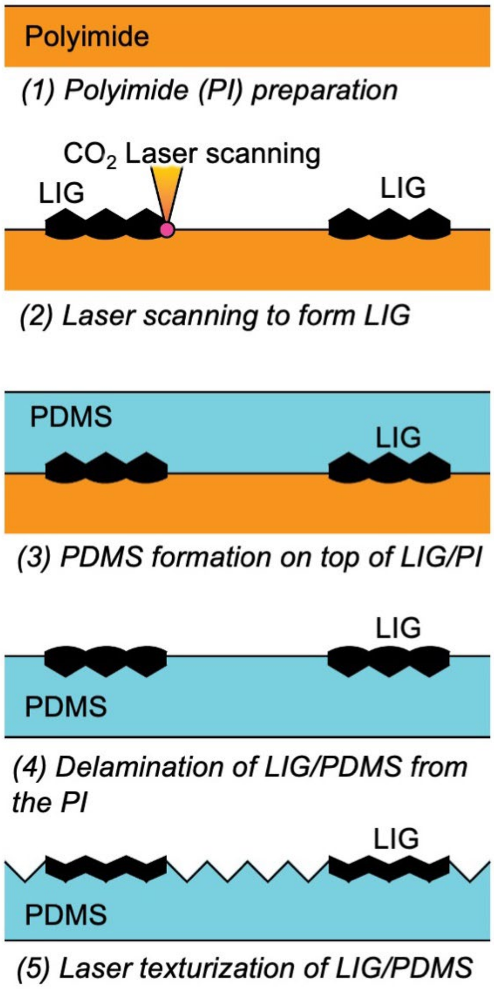

Figure S1. Device fabrication process.

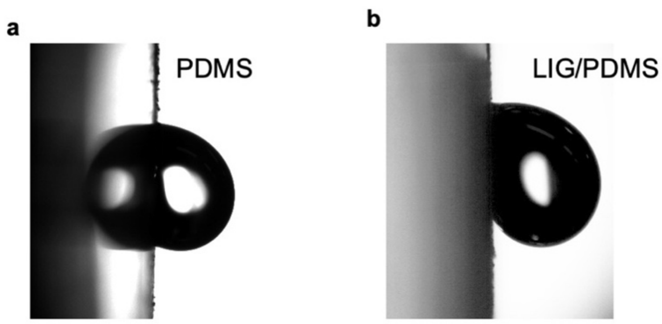

Figure S2. Photos of water droplet at a 90° tilt angle on (a) PDMS and (b) LIG/PDMS.

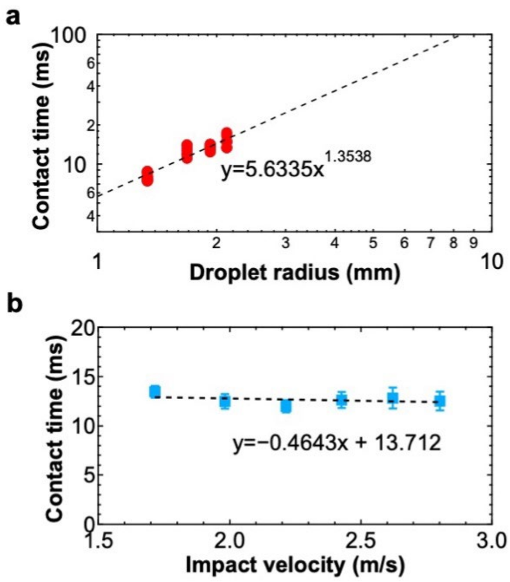

Figure S3. Contact times at different (a) droplet radii and (b) impact velocities.

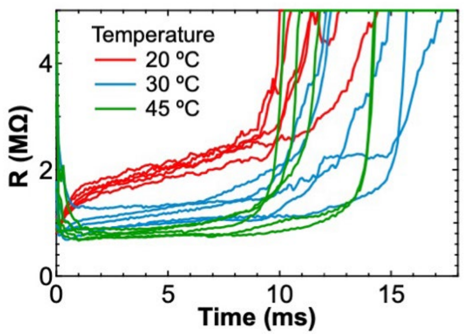

Figure S4. Time series of the resistance at different temperature using a water droplet volume of 30µL, a wind velocity of 0 m/s, and a tilt of 20°

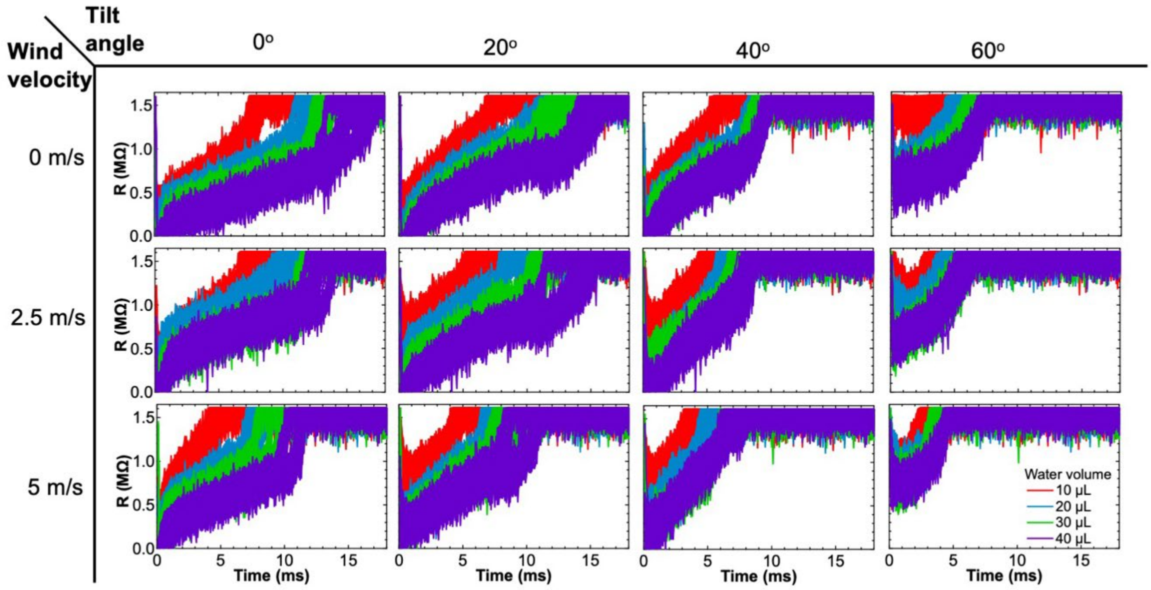

Figure S5. Datasets after data augmentation at different wind velocities, volumes, and tilt angles.

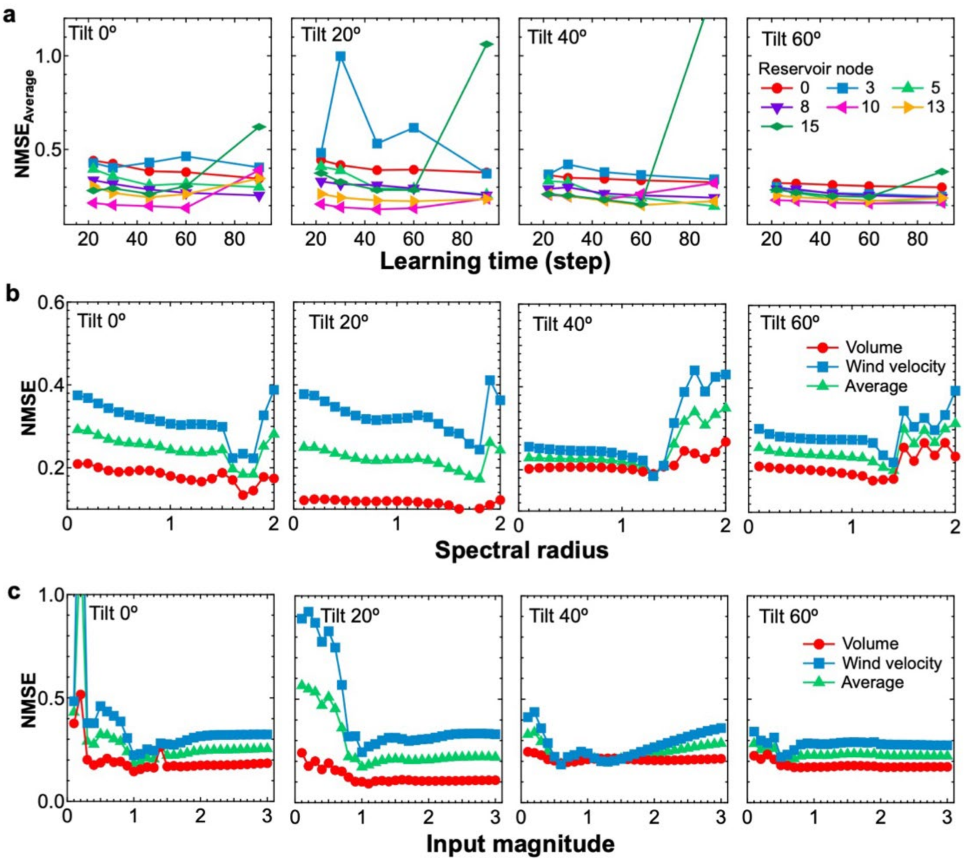

Figure S6. (a) NMSE$_{Average}$ as a function of time-multiplexing at different tilt angles. (b) NMSE as a function of the spectral radius at different tilt angles. (c) NMSE as a function of the input magnitude at different tilt angles.

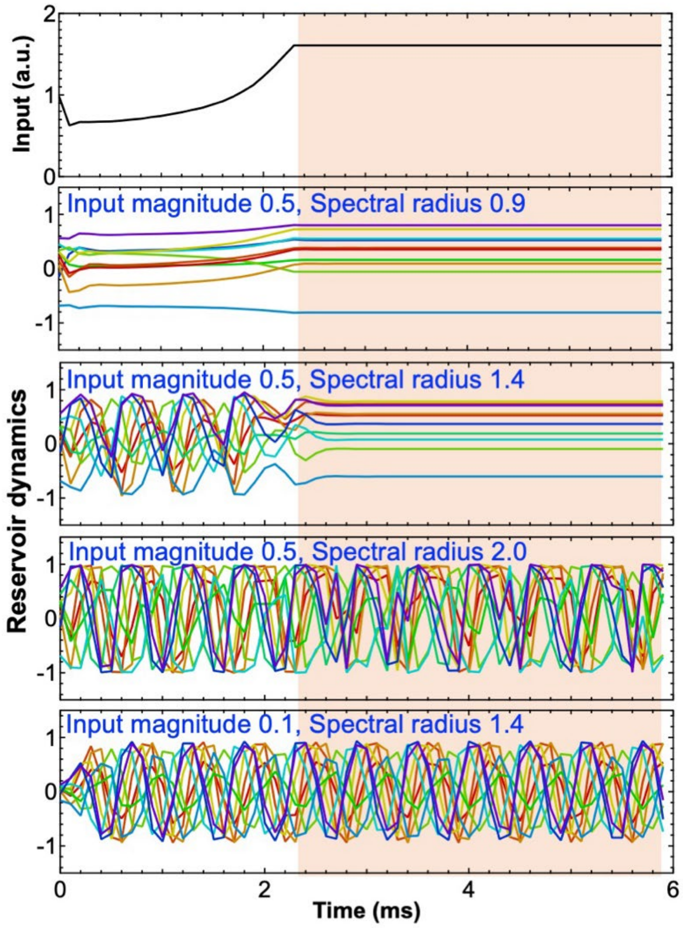

Figure S7. Time series of the input and reservoir dynamics at different input magnitudes and spectral radii.

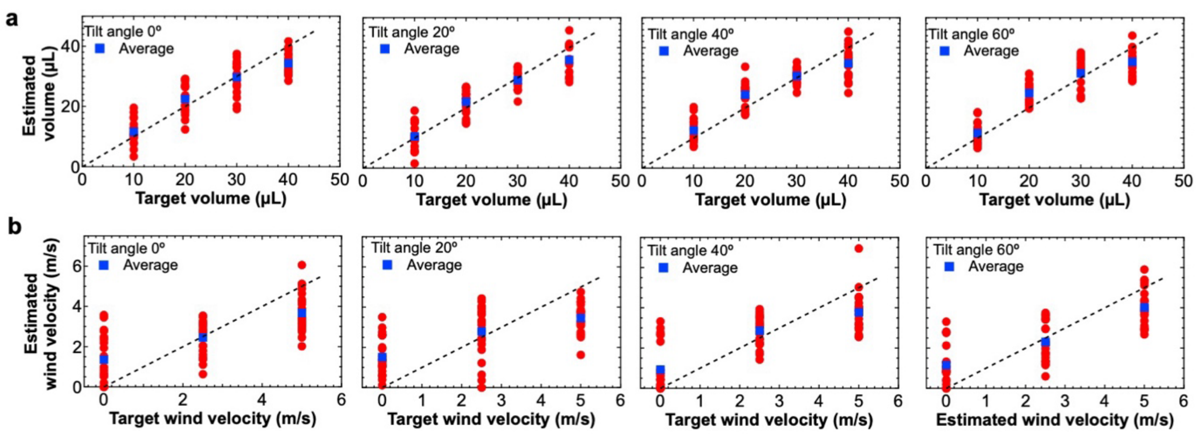

Figure S8. (a) Volume and (b) wind velocity estimated against the target at each tilt angle without using ESN (only input series).

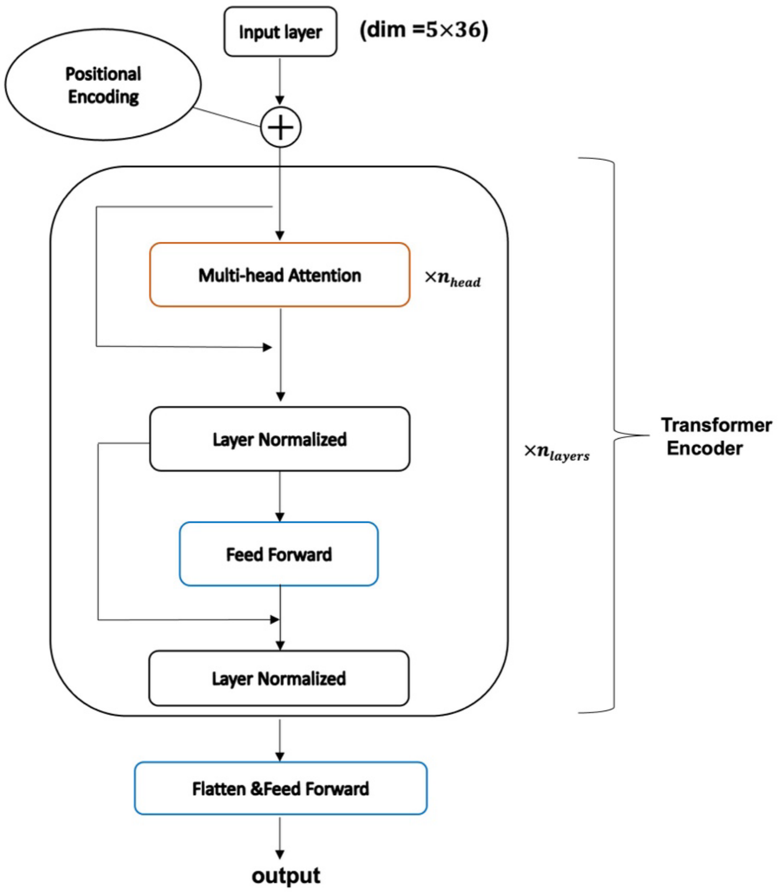

Figure S9. Analyses flow of the transformer used in this study.

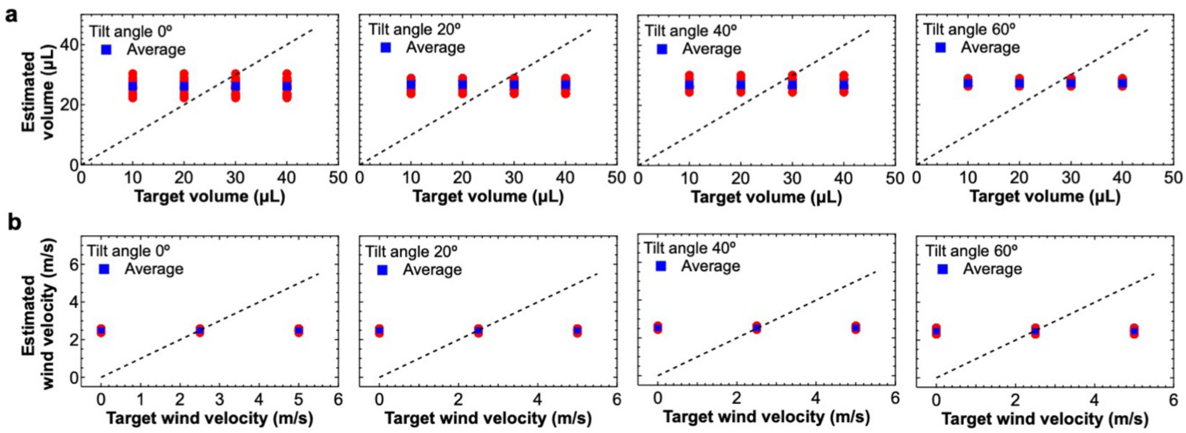

Figure S10. (a) Volume and (b) wind velocity against the target at each tilt angle estimated using the transformer.

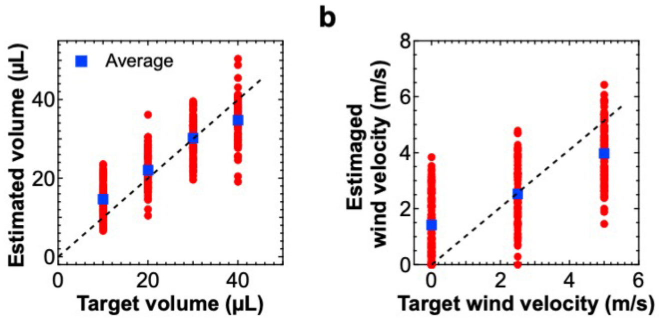

Figure S11. (a) Estimated volume and (b) wind velocity against the targets using all datasets simultaneously, including the tilt angle.

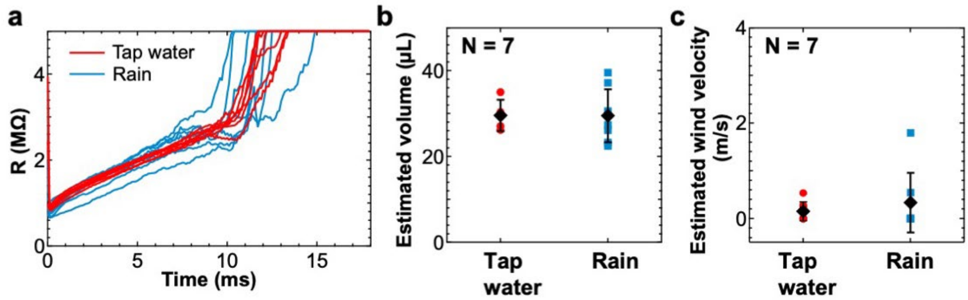

Figure S12. (a) Time series of the resistance using rainwater and tap water for comparison. (b) Estimated volume and (c) estimated wind velocity using rainwater and tap water with error bars against target values for a volume of 30 µL, a wind velocity of 0 m/s, and a tilt of 20° (N=7 for each condition).

Table S1. Hyperparameters for the optimum ESN.

	Tilt 0°	Tilt 20°	Tilt 40°	Tilt 60°	All tilt angles
Reservoir node	**10**	**10**	**5**	**10**	**10**
Time-multiplexing	60	45	90	60	90
Input magnitude	1.0	1.0	0.6	0.5	0.6
Spectral radius	1.8	1.8	1.3	1.4	1.4
Ridge parameter	0.490906	0.589166	0.032416	0.024993	0.053607

Table S2. Hyperparameters for the transformer used in this study.

	Tilt 0°		Tilt 20°		Tilt 40°		Tilt 60°	
	volume	Wind velocity	volume	Wind velocity	volume	Wind velocity	volume	Wind velocity
n_{layers}	7	4	4	8	8	7	8	4
n_{head}	6	18	18	18	18	9	6	12

References

[1] A. Vaswani, N. Shazeer, N. Parmar, J. Uszkoreit, L. Jones, A. N. Gomez, L. Kaiser, I. Polosukhin, *31st Conf. Neural Information Processing Systems (NIPS 2017)* **2017**.

[2] H. Zhou, S. Zhang, J. Peng, S. Zhang, J. Li, H. Xiong, W. Zhang, Proceedings of the AAAI conference on artificial intelligence, 2021, 35(12), 11106-11115.

[3] Y. Yuan, L. Lin, IEEE J. Sel. Top. Appl. Earth Obs. Remote Sens. 2021, 14, 474-487.

[4] Y. Jin, L. Hou, Y. Chen, Neurocomputing, 2022, 494, 379-395.